The self-complementary effect through strong orbital coupling in ultrathin high-entropy alloy nanowires boosting pH-universal multifunctional electrocatalysis

Hongdong Li [a], Mingzi Sun [c], Yue Pan [a], Juan Xiong [a], Haoyang Du [a], Yaodong Yu [a], Shouhua Feng [a], Zhenjiang Li [d], Jianping Lai [a,*], Bolong Huang [c,*], Lei Wang [a,b,**]

[a] Key Laboratory of Eco-Chemical Engineering, Taishan Scholar Advantage and Characteristic Discipline Team of Eco-Chemical Process and Technology, College of Chemistry and Molecular Engineering, Qingdao University of Science and Technology, Qingdao 266042, PR China
[b] Shandong Engineering Research Center for Marine Environment Corrosion and Safety Protection, College of Environment and Safety Engineering, Qingdao University of Science and Technology, Qingdao 266042, PR China
[c] Department of Applied Biology and Chemical Technology, The Hong Kong Polytechnic University, Hung Hom, Kowloon, Hong Kong Special Administrative Region of China
[d] College of Materials Science and Engineering, Qingdao University of Science and Technology, Qingdao, Shandong 266061, PR China

ARTICLE INFO

ABSTRACT

Rational control of the compositions, morphologies and sizes of electrocatalyst are the key factors for achieving high performance of electrocatalytic reactions. Herein, a newly ultrathin PtRuRhCoNi high-entropy alloy nanowires (HEA-NWs) (~1.6 nm) catalyst is designed. The PtRuRhCoNi NWs/C achieved high mass activity of 7.68 A mg_{PtRuRh}^{-1}, ultrahigh C1 selectivity of 78% for ethanol oxidation reaction. For hydrogen evolution reaction, the PtRuRhCoNi NWs/C also reached high mass activity, turnover frequency (11.99 A mg_{PtRuRh}^{-1}, 31.9 s^{-1}, 0.5 M H_2SO_4 and 8.07 A mg_{PtRuRh}^{-1}, 26.7 s^{-1}, 1 M KOH at -0.05 V *vs.* RHE) and stability. Theoretical calculations demonstrated that the excellent electroactivity of HEA is benefited by the self-complementary effect through strong orbital coupling, which maximized the electroactivity towards both oxidation and reduction and preferred binding of key intermediate. The design of pH-universal multifunctional catalyst by rational control of the compositions, morphologies and sizes strategy can facilitate the research of advanced catalysts.

1. Introduction

Platinum (Pt) is considered as an advanced electrocatalyst for hydrogen evolution reaction (HER) and alcohol oxidation reaction (AOR) [1–5]. However, CO poisoning on the surface of Pt catalysts inevitably inhibits the catalytic performance in AOR [3,6]. In the ethanol oxidation reaction (EOR), the low CO_2 selectivity and current density in the low potential range are still fundamental issues [7–9]. So far, scientists have tried strategies such as alloys, nanostructures, defects, and composite materials [3,9–18]. However, these methods cannot effectively solve the above problems in EOR well. For the hydrogen evolution reaction (HER), Pt catalysts have low overpotential and fast reaction kinetics in acidic conditions [2]. However, the

agglomeration and dissolution of metal nanoparticles during the catalysis catalytic process can lead to a rapid decline in catalytic performance [2,19]. In order to suppress the agglomeration of metal catalysts to ensure long-term operation, carbon substrates are often used as a support for dispersing metal catalysts [20]. In alkaline solution, H * is generated by the process of water dissociation on Pt catalyst, but this process is very sluggish on Pt, resulting in two orders of magnitude lower HER activity of Pt catalyst than in acidic medium [2,21–23]. Although countless highly active and stable HER electrocatalysts have been synthesized, there is still room for improvement in Pt-based catalysts to enhance the HER activity, kinetics and stability in both acidic and alkaline solutions.

In general, EOR has two reaction pathways, namely the C1 pathway

and the C2 pathway. In most cases, incomplete oxidation of the C2 pathway is prevalent, producing acetic acid and acetaldehyde [3,13]. While the complete oxidation of ethanol by the C1 pathway is 12-electron process and requires cleavage of the C-C bond, CO_{ad} is strongly adsorbed on the catalyst surface and cannot be removed by oxidation at low potential, which hinders the further adsorption of reactants, thereby inhibiting the current density and CO_2 selectivity [3,13,24]. Therefore, Pt-based catalysts should be designed to easily break the C-C bond (introducing Rh, Ir *etc.*), while also providing sufficient *OH species for oxidation of C1 species (introducing Ru, Co and Ni oxophilic metals) to facilitate complete oxidation at low potentials [3,24,25]. In addition, the HER process mainly involves the reaction of protons (acidic electrolyte: hydronium ions and alkaline electrolyte: water molecules) with electrons to generate *H intermediates, *H intermediates adsorb and recombine into molecular hydrogen, finally, H_2 is desorbed [2,24]. In acidic media, other active sites (Ru, Rh *etc.*) can be introduced and the electronic structure can be adjusted to optimize the H * adsorption of the catalyst and further improve its intrinsic activity. In alkaline media, active sites with different functions can be designed to lower the water dissociation barrier (Ru, Co and Ni oxophilic metals with good OH* sites promote water dissociation), and improve the catalyst-H interaction to enhance the reaction kinetics [21,22,24,26–28]. Based on the above analysis, the development of multicomponent catalysts with abundant active sites is the key to improve EOR and HER performance.

Notably, high-entropy alloys (HEAs) have received extensive attention in the field of catalysis due to their tunable compositions and high stability in corrosive media [24,29–40]. In addition, precise control of material structure at the nanoscale is another powerful means to tune catalyst performance. The one-dimensional nanomaterials serve as a class of high-performance electrocatalysts due to the exposure of more active sites, high specific surface area, and excellent resistance to dissolution [41–46]. Combining the advantages of one-dimensional nanowire structure and the multi-component properties of HEAs, which can not only tune the kinetics of the reaction but also improve the selectivity and stability, provide an ideal model for designing catalysts. Therefore, precise control of the compositions, morphologies and sizes of HEAs may enable high activity, selectivity and durability for AOR and HER in acidic and alkaline solutions. However, this is still extremely challenging.

In this work, we design and synthesize the PtRuRhCoNi HEA ultra-thin nanowires (NWs) and achieve excellent activity and durability for EOR/MOR and HER in acidic and alkaline solutions due to the complementary effect of the electronic structures. For alcohol oxidation, the PtRuRhCoNi NWs/C exhibits high activity, robust stability for EOR/MOR with negligible activity decay after 2000 cycles and CO toxicity resistance compared to PtRuRhCoNi NPs/C, Pt NWs/C and commercial Pt/C. Importantly, the PtRuRhCoNi NWs/C shows high C-C bond breaking capacity in EOR, with C1 selectivity up to 78% at low potential, which has the highest C1 selectivity among the reported catalysts (Table S5). As HER electrocatalyst, the PtRuRhCoNi NWs/C displays a low overpotential of 13 and 15 mV in 0.5 M H_2SO_4 and 1 M KOH solutions, respectively. And the mass activity of the PtRuRhCoNi NWs/C is much higher than those of PtRuRhCoNi NPs/C, Pt NWs/C and commercial Pt/C catalysts. In addition, the PtRuRhCoNi NWs/C also shows ultrahigh turnover frequency (TOF) and excellent stability with no decay after 10,000 cycles or 200 h. The PtRuRhCoNi NWs/C is one of the best HER catalysts (Table S7 and Table S8). Density functional theory (DFT) calculations have revealed the complementary effect of the electronic structures in the HEA, which leads to both strong oxidation and reduction capability of the electrocatalyst. Meanwhile, such unique electronic structures also resulted in low energy barriers for both EOR and HER and high durability for electrocatalysis.

2. Experimental section

2.1. Materials

Platinum (II) acetylacetonate (Pt(acac)$_2$, 97%), rhodium(III) acetylacetonate (Rh(acac)$_3$, 97%) nickel (II) acetylacetonate (Ni(acac)$_2$, 95%), molybdenumhexacarbonyl (Mo(CO)$_6$, 98%), and oleylamine (OAm, > 70%) were bought from Sigma-Aldrich. Ruthenium(III) acetylacetonate (Ru(acac)$_3$, 97%) was purchased from Macklin. Cobalt (II) acetylacetonate (Co(acac)$_2$, 98%), Nafion solution (5 wt%) were supplied by Alfa Aesar. Methanol, cyclohexane, ethanol, and isopropanol were bought from Beijing Tongguang Fine Chemicals Company. Hexadecyl trimethyl ammonium Bromide (CTAB, 99%) and potassium hydroxide (KOH, 90%) was purchased from Aladdin.

2.2. Materials synthesis

2.2.1. Preparation of high-entropy alloy PtRuRhCoNi

Pt(acac)$_2$ (25 mg), Ru(acac)$_3$ (10 mg), Rh(acac)$_3$ (10 mg), Co(acac)$_2$ (6.6 mg), Ni(acac)$_2$ (6.6 mg), Mo(CO)$_6$ (33 mg) and CTAB (80 mg) was added into oleylamine (5 mL) in a 15 mL vial. The vial was heated to 200 °C and the reaction was kept 2 h under magnetic stirring at 400 rpm. The black colloidal products were collected by centrifugation and washed two times with an ethanol/cyclohexane mixture. Finally, the black colloidal products (PtRuRhCoNi HEA-NWs) were kept in cyclohexane for further use. In addition, the PtRuRhCoNi HEA nanoparticles (NPs) were synthesized under conditions similar to HEA-NWs without CTAB. The Pt NWs were prepared by using Pt(acac)$_2$ in the same way.

2.2.2. Preparation of PtRuRhCoNi/C

The obtained 0.5 mg HEA-NWs or HEA-NPs dispersed in 10 mL cyclohexane was mixed with 4.5 mg of carbon (Ketjen Black-300) in 10 mL ethanol under sonication for 1 h, and then the product was collected *via* centrifugation with ethanol.

2.3. Materials characterizations

The material morphology was examined by the transmission electron microscopy (TEM) and high-resolution TEM (HRTEM) (FEI Tecnai-G2 F30 at an accelerating voltage of 300 KV). Powder X-ray diffraction (XRD) spectra were recorded on X′Pert-PRO MPD diffractometer operating at 40 kV and 40 mA with Cu Kα radiation. The X-ray photoelectron spectra (XPS) analyses were carried out with Axis Supra spectrometer using a monochromatic Al Kα source (15 mA, 14 kV). The detection of acetic acid and acetaldehyde were conducted by gas chromatography (GC, SHIMADZU GC2014C). The intermediate products were detected by *in-situ* FTIR (Thermo iS50 FT-IR).

2.4. Electrochemical measurements

The different catalysts were dispersed in a mixture of ultrapure water, isopropanol, and Nafion solution (*v:v:v* = 1:1:0.01) to reach a homogeneous catalyst ink with a concentration of 1 mg mL^{-1} by sonication for 1 h.

Electrochemical measurements were conducted on a CHI 660E Electrochemical Workstation (Shanghai Chenhua Instrument Corporation, China) in a conventional three-electrode cell. The graphite rod electrode is the counter electrode and a saturated calomel electrode (SCE) is the reference electrode. The working electrode was a glassy carbon electrode (GCE, diameter: 3 mm, area: 0.07065 cm^2). 10 µL of the catalyst (PtRuRhCoNi/C, Pt/C (20 wt%), Pt NWs/C (20 wt%)) was dropped onto the GCE surface for further electrochemical tests. All the potentials reported in this work were converted to the reversible hydrogen electrode (RHE).

2.4.1. Ethanol oxidation reaction (EOR) and methanol oxidation reaction (MOR) measurements

The CVs for EOR/MOR were conducted in N_2-saturated 1 M KOH + 1 M C_2H_5OH (0.5 M H_2SO_4 + 1 M C_2H_5OH, 1 M KOH + 1 M CH_3OH) solution between 0.05 and 1.25 V *vs.* RHE with a scan rate of 50 mV s^{-1}. For the EOR stability tests, chronoamperometric tests were performed at a fixed potential, and 2000th CVs were also performed to evaluate the stability of catalysts. 20% Pt/C catalyst was also dropped on the GCE as a reference catalyst for electrochemical tests under the same conditions.

2.4.2. CO stripping measurements

CO stripping curves were conducted in 0.5 M H_2SO_4 solution (or 1 M KOH solution). Before the tests, 0.5 M H_2SO_4 (or 1 M KOH solution) was first deaerated with high-purity N_2. Then, CO was bubbled into the cell for 15 min while the potential of the working electrode was held at a constant potential of 0.1 V *vs.* RHE. Then N_2 was bubbled into the system for 15 min to remove CO gas. After that, CO stripping curves were recorded between 0.05 and 1.20 V *vs.* RHE at a scan rate of 50 mV s^{-1}.

2.4.3. The electrochemical surface area (ECSA) calculation

The ECSA was estimated by CO stripping test. Assuming that the Coulomb charge required for CO monolayer oxidation is 0.42 mC cm^{-2}.

$$\text{ECSA}\left(S^{-1}\right) = \frac{Q_{CO}}{0.42 \quad mC \quad cm^{-2} * m_{noble}}$$

2.4.4. Hydrogen evolution reaction (HER) measurements

The HER performance of the catalysts was evaluated by linear sweep voltammetry (LSV) with a scan rate of 5 mV s^{-1} in N_2-saturated 0.5 M H_2SO_4 solution and 1 M KOH solution, and all polarization curves were 95% iR-corrected. The durability tests were performed in 0.5 M H_2SO_4 solution and 1.0 M KOH solution using the chronoamperometric method. And 1000th/10,000th CVs were also measured to evaluate the stability of catalysts. EIS was tested from 100,000–0.01 Hz, and the amplitude is 5 mV. 20% Pt/C catalyst was also dropped on the GCE as a reference catalyst for electrochemical tests under the same conditions.

Active sites calculations: The active sites of PtRuRhCoNi NWs/C and other samples were calculated by CO stripping measurement.

$$n = \frac{Q_{CO}}{2 * F}$$

Q_{CO} represents CO stripping charge, F is Faraday's constant (96,485 C mol^{-1}).

TOF calculation:

$$\text{TOF}\left(S^{-1}\right) = \frac{I}{2 * F * n}$$

The n is the number of active sites, the number 2 represents two electrons (produce one hydrogen molecule), F is Faraday's constant (96,485 C mol^{-1}), I(A) is the current measured at a specific potential during LSV measurement.

2.5. EOR products analysis and apparent faraday efficiency calculation

The EOR products analyses mainly focused on the carbonate (C1 product) and acetate and acetaldehyde (C2 product).

$$\text{FE}_{C2} = \frac{C_{C2} * V * n * F}{Q}$$

$$\text{FE}_{C1} = 1 - \text{FE}_{C2}$$

where FE_{C2} and FE_{C1} represent the faraday efficiency of the C2 and C1 pathways in the EOR. C_{C2} is the concentration of generated acetate and acetaldehyde by GC, n is the total moles of acetaldehyde or acetate, F is the faraday constant (96,485 C mol^{-1}), and Q is the total charge.

2.6. Density functional theory calculations

To investigate the performances of PtRuRhCoNi HEA, DFT calculations have been introduced through the CASTEP packages [47]. To reach the accurate descriptions of exchange-correlation interactions, we have chosen the generalized gradient approximation (GGA) and Perdew-Burke-Ernzerhof (PBE) functionals [48–50]. The plane-wave basis cutoff energy has been set to 380 eV and the ultrasoft pseudopotentials have been applied for all the geometry optimizations. In addition, the Broyden-Fletcher-Goldfarb-Shannon (BFGS) algorithm [51] and the coarse quality setting of k-points are used for all the energy minimizations. For all the geometry optimization, we have introduced 20 Å vacuum space in the z-axis for all the models. The convergence criteria have been set for all the geometry optimizations as follows: the Hellmann-Feynman forces should not exceed 0.001 eV Å^{-1}, the total energy difference should not be over 5×10^{-5} eV atom^{-1}, and the inter-ionic displacement should be less than 0.005 Å. The PtRuRhCoNi HEA model has been built based on Pt (111) surface with six layer thickness including 150 randomly distributed atoms. The site-dependent projected partial density of states (PDOSs) are demonstrated by selecting one atom of each element from the bottom layer towards the surface layer. For the surface layer, the distorted sites with ower coordination are considered as the surface edge sites. Fort stability of the PtRuRhCoNi HEA, we have carried out molecule dynamic (MD) simulations under the NVT (constant pressure and volume) condition at 300 K and standard pressure. The time step is 0.5 fs and the total simulation time is 2.5 ps with 5000 simulation steps. The value of the mean square displacements (MSD) for a given time of each element has been demonstrated based on the average displacement over the time.

3. Results & discussion

3.1. Preparation and characterizations of catalysts

In the synthesis of HEA-NWs, platinum (II) acetylacetonate (Pt(acac)$_2$), ruthenium(III) acetylacetonate (Ru(acac)$_3$), rhodium (III) acetylacetonate (Rh(acac)$_3$), cobalt (II) acetylacetonate (Co(acac)$_2$), and nickel (II) acetylacetonate (Ni(acac)$_2$) are used as metal precursors, hexadecyl trimethyl ammonium bromide (CTAB) as structural guide agent, molybdenumhexacarbonyl (Mo(CO)$_6$) and oleamine (OAm) as reducing and solvent agent. After ultrasonic treatment, the mixture was heated to 200 °C in an oil bath for 2 h. Transmission electron microscope (TEM) images (Fig. 1**a** and **b**) show that the prepared HEA sample is ultrathin NWs structure, and the average diameter of PtRuRhCoNi NWs is about 1.6 nm. For comparison, Pt NWs was also prepared without the addition of other metal precursors (Fig. S1). The high resolution TEM (HRTEM, Fig. 1**c**) image shows a lattice spacing of 0.217 nm, corresponding to the (111) lattice fringe of XRD pattern (Fig. 1**d**), the NWs show a typical fcc structure, the broadened diffraction peak indicates the ultrathin characteristic [33,52]. In addition, TEM-EDS mapping (Fig. 1**e**) and line scanning (Fig. 1**f**) show that Pt, Ru, Rh, Co and Ni were evenly distributed in the NWs. X-ray photoelectron spectroscopy (XPS) also shows the presence of Pt, Ru, Rh, Co and Ni elements, where all the metals in HEA-NWs were mixed in metallic and oxidized states (Fig. S2). In addition, the inductively coupled plasma optical emission spectroscopy (ICP-OES) result shows that the atomic ratio of Pt, Ru, Rh, Co and Ni is 32:11:25:12:20.

To probe the formation mechanism of PtRuRhCoNi NWs, we investigated the morphologies and compositional evolution of the samples obtained at different reaction times. After 30 s reaction, NPs and shorter NWs were observed (Fig. S3a). From the Fig. S3b-f, with the prolongation of the reaction time, the NWs gradually became longer, accompanied by the reduction of other metals. After 2 h, the morphology and atomic ratio of the PtRuRhCoNi NWs remained unchanged. In addition, the influence of other factors on synthesis was also discussed. As shown in Fig. S4a, in the absence of CTAB, the product was small NPs.
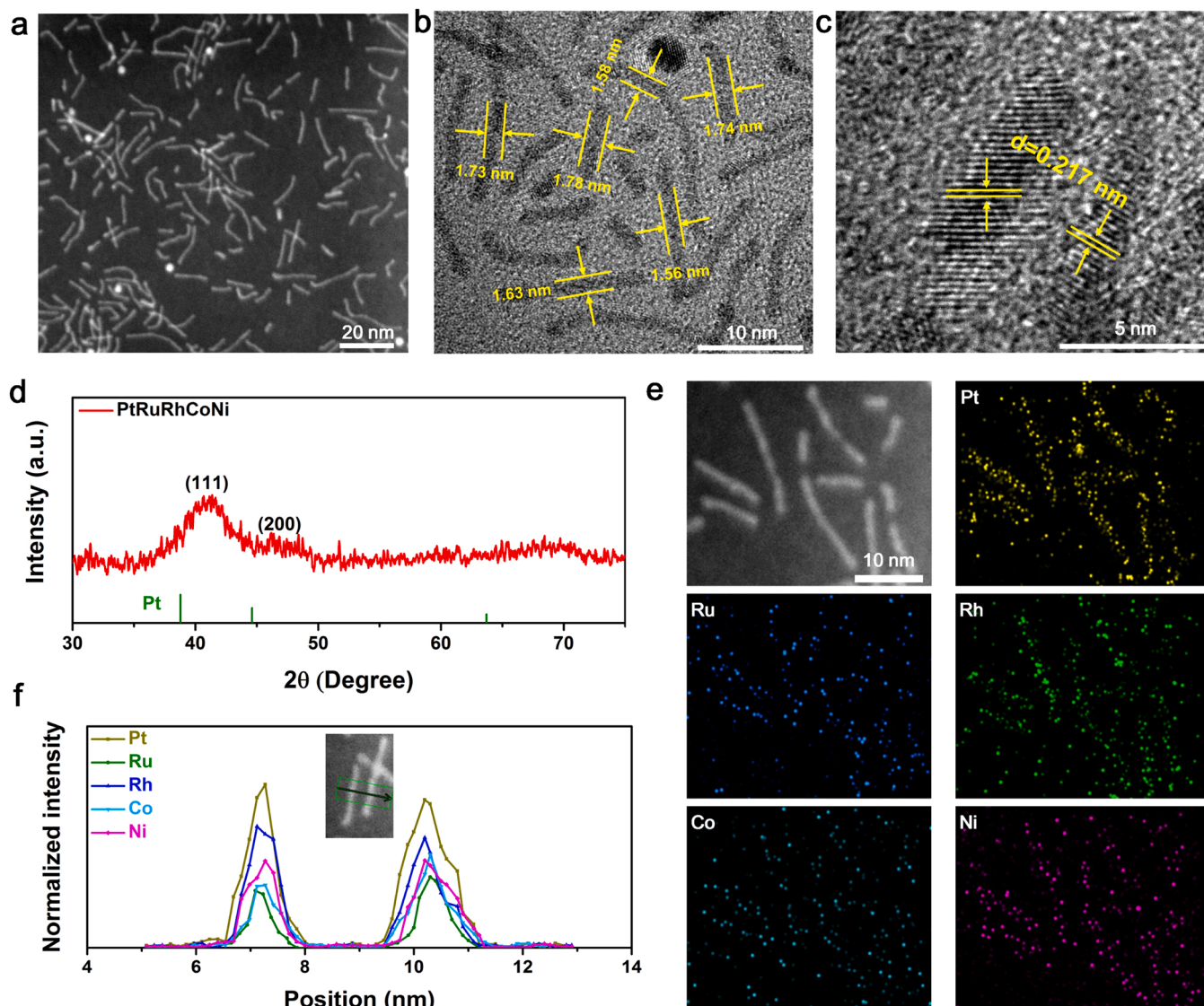
Fig. 1. (a) HAADF-STEM image, (b) The TEM image, (c) The HRTEM image, (d) The XRD pattern, (e) The elemental mapping, and (f) EDS line-scanning profile of PtRuRhCoNi NWs.

However, irregular and aggregated NPs with large size were produced without the addition of $Mo(CO)_6$ (Fig. S4b). These results indicate that the morphological evolution process of PtRuRhCoNi NWs is almost identical to that of previously reported NWs, with CTAB acting as structure directing agent to guide the growth of NWs, and $Mo(CO)_6$ acting as reducing agent to control the reaction rate [5,33].

3.2. Electrocatalytic performance for AOR

Before electrochemical test, the PtRuRhCoNi NWs and PtRuRhCoNi NPs were loaded on carbon black (Fig. S5). Firstly, the electrocatalytic performance of EOR in alkaline solution was studied. The electrochemical surface area (ECSA) of PtRuRhCoNi NWs/C, PtRuRhCoNi NPs/C, Pt NWs/C and commercial Pt/C were 75.1 m^2 g_{PtRuRh}^{-1}, 74.8 m^2 g_{PtRuRh}^{-1}, 71.4 m^2 g_{Pt}^{-1} and 66.6 m^2 g_{Pt}^{-1}, respectively (Table S1). By cyclic voltammetry (CV) tests (Fig. 2**a** and S6), PtRuRhCoNi NWs/C catalyst showed higher EOR activity than PtRuRhCoNi NPs/C, Pt NWs/C and commercial Pt/C. The mass activity and specific activity of PtRuRhCoNi NWs/C were 7.68 A mg_{PtRuRh}^{-1} (9.50 A mg_{Pt}^{-1}) and 7.55 mA cm_{PtRuRh}^{-2} (Fig. 2**b** and Table S2), the mass activity is 1.1, 4.1, and 6.7 times higher than those of PtRuRhCoNi NPs/C (7.04 A mg_{PtRuRh}^{-1}, 8.46 A mg_{Pt}^{-1}), Pt

NWs/C (1.86 A mg_{Pt}^{-1}) and commercial Pt/C (1.15 A mg_{Pt}^{-1}), and it is the one of the best among reported EOR catalysts (Table S5). In CO stripping test, PtRuRhCoNi NWs/C showed a negative shift of CO oxidation peak compared with PtRuRhCoNi NPs/C, Pt NWs/C and commercial Pt/C, indicating that CO species can be oxidatively removed at a lower potential, enhancing their anti-toxicity and promoting oxidation (Fig. S7). After 2000 CV cycles, the mass activity of PtRuRhCoNi NWs/C could be maintained at more than 96.8%, which was higher than PtRuRhCoNi NPs/C, Pt NWs/C and commercial Pt/C (Fig. 2**c** and **S8**). Meanwhile, PtRuRhCoNi NWs/C maintained high mass activity after 3600 s chronoamperometric (CA) tests (Fig. 2**d**). Moreover, the catalytic activity of PtRuRhCoNi NWs/C could be restored by changing the fresh working electrolyte in cycle CA tests (Fig. 2**e**). In addition, we also compared the catalytic performances of PtRuRhCoNi NWs and PtRuRhCoNi NWs/C for EOR. From the Fig. S9a, the initial EOR activity of the PtRuRhCoNi NWs catalyst without carbon support is close to that of PtRuRhCoNi NWs/C. However, the activity of the PtRuRhCoNi NWs catalyst decreased significantly after 2000 cycles, which may be due to the agglomeration of the PtRuRhCoNi NWs during the testing process (Fig. S9b-c). Importantly, the structure of PtRuRhCoNi NWs/C is well maintained after stability tests (Figs. S10-S11). And the element ratio of
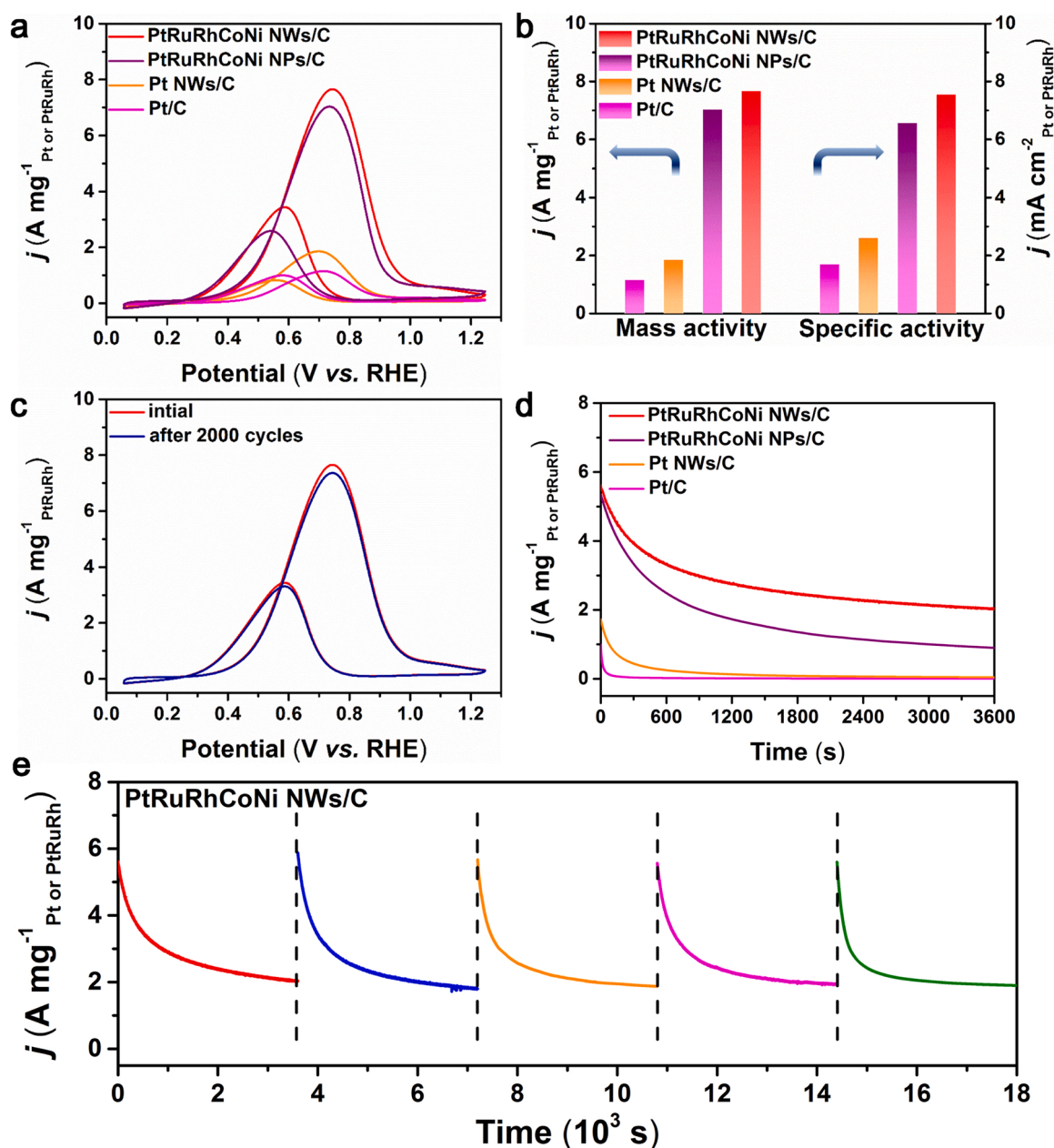
Fig. 2. EOR performance of different electrocatalysts in 1 M KOH + 1 M C$_2$H$_5$OH. (a) Mass activity CVs for EOR. (b) Corresponding histogram of specific and mass activities. (c) CV curves before and after 2000 cycles of PtRuRhCoNi NWs/C. (d) Chronoamperometric (CA) tests for EOR. and (e) Long-time durability of PtRuRhCoNi NWs/C.

PtRuRhCoNi NWs/C catalyst did not obviously change after stability test (Table S3). These results indicate that PtRuRhCoNi NWs/C catalyst has excellent EOR activity and stability. This also illustrates the importance of carbon black as a support, which can inhibit the agglomeration of PtRuRhCoNi NWs and ensure the stability during long-term operation. In addition, the electrocatalytic performance of EOR in acidic solution was also studied. In 0.5 M H$_2$SO$_4$ + 1 M C$_2$H$_5$OH, PtRuRhCoNi NWs/C also show excellent catalytic activity and stability (Fig. S12). The geometric area activity and mass activity of PtRuRhCoNi NWs/C can reach 15.7 mA cm^{-2} and 1.52 A mg$_{PtRuRh}^{-1}$, which is higher than those of PtRuRhCoNi NPs/C, Pt NWs/C and commercial Pt/C. In addition, the CO resistance of PtRuRhCoNi NWs/C is also better than PtRuRhCoNi NPs/C, Pt NWs/C and commercial Pt/C in acidic media (Fig. S13).

As shown in Fig. 3a, the reaction path of EOR is complex due to multiple dehydrogenation and oxidation of ethanol [13,17,18]. In most cases, ethanol is partially oxidized to acetate and acetaldehyde through

the C2 pathway. However, ethanol is required to transfer 12 electrons for complete oxidation to CO$_2$ along the C1 path in the direct fuel cell [13,17]. Furthermore, we conducted *in-situ* FTIR spectroscopy of PtRuRhCoNi NWs/C and commercial Pt/C in EOR (Fig. 3b-c). Ethanol consumption was confirmed by the stretching vibration of the C-O bond of ethanol at 1043 cm^{-1} and 1085 cm^{-1} in the spectra [16–18]. In addition, two bonds at 1550 and 1416 cm^{-1} correspond to asymmetrical and symmetric O-C-O bonds stretching vibrations from acetate (CH$_3$COO$^-$), the bond at 1346 cm^{-1} corresponds to the -CH$_3$ bending vibration in CH$_3$COO$^-$ [16,17]. For PtRuRhCoNi NWs/C, the bands at 1550 and 1416 cm^{-1} begin to drop when the voltage is raised to 0.8 V *vs.* RHE, while the bands of commercial Pt/C drop at 1.0 V *vs.* RHE. Therefore, PtRuRhCoNi NWs/C has a better ability to inhibit CH$_3$COO$^-$ formation. In addition, CO$_2$ partially dissolves in an alkaline electrolyte to form CO$_3^{2-}$ (1390 cm^{-1}). The band at 1416 cm^{-1} shows higher intensity due to CO$_3^{2-}$ overlap at ~1390 cm^{-1}. The bond at 2345 cm^{-1} is
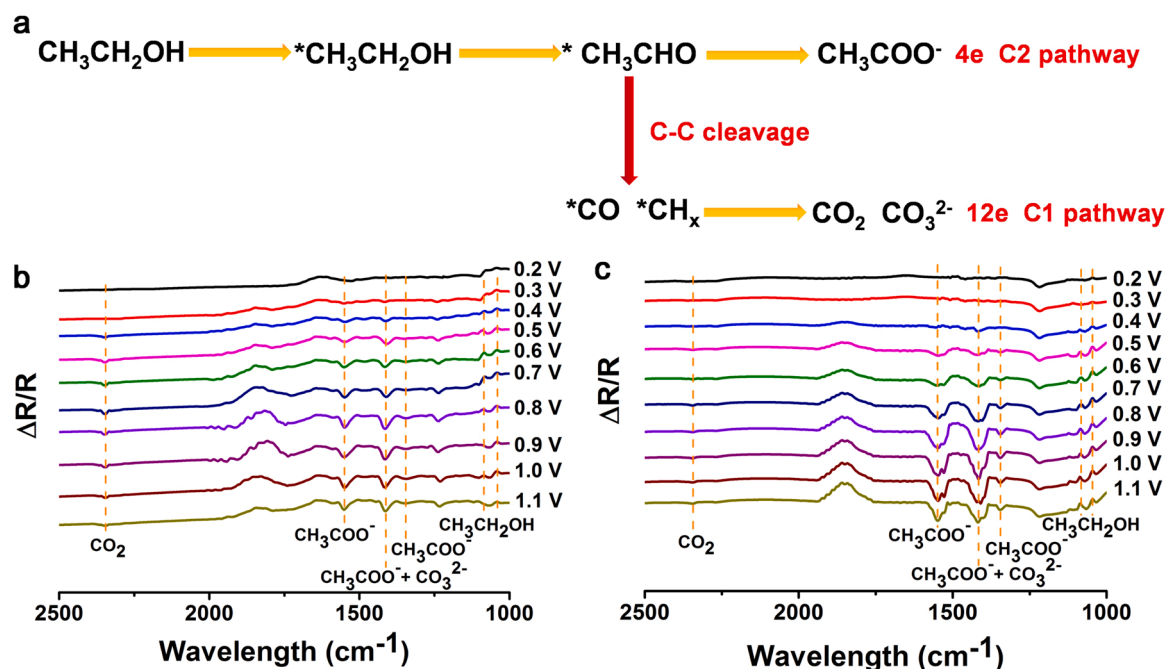
Fig. 3. (a) Scheme of active EOR pathways. In situ FTIR spectrum of EOR on (b) PtRuRhCoNi NWs/C and (c) commercial Pt/C.

associated with the O-C-O asymmetric stretching of CO_2 through the C1 pathway, the bond intensity of PtRuRhCoNi NWs/C is much higher than that of commercial Pt/C. From the *in-situ* FTIR spectroscopy, ethanol oxidation in PtRuRhCoNi NWs/C occurs at low potentials, revealing its accelerated reaction kinetics. Those results indicate that following the C1 pathway is favorable for C-C bond splitting to form CO_2 on PtRuRhCoNi NWs/C.

The oxidation products of PtRuRhCoNi NWs/C catalyst were further analyzed by gas chromatography (GC). Acetate and acetaldehyde were the main C2 products. By calculating with the C2 standard concentration sample (Fig. S14), the Faraday efficiency of the C1 pathway (CO_2) of PtRuRhCoNi NWs/C is about 48%, 63% and 78% deduced at 0.5 V, 0.6 V and 0.7 V *vs.* RHE, respectively, which is much higher than that of commercial Pt/C (Fig. S15). And it has the highest C1 selectivity among the reported EOR catalysts (Table S5). This indicates that PtRuRhCoNi NWs/C has a higher C-C cleavage capacity to produce C1 products. The high activity and C1 selectivity are attributed to the synergistic effect of electronic structures from different elements in the HEAs. Among them, Pt catalyst has a higher activity for EOR [11,13,14,31,53]. Rh catalysts can promote dehydrogenation or C-C cleavage at low potential, but further oxidation is difficult [8,18,31,53,54]. Ru not only has high EOR activity, but also can greatly promote the C-C bond breaking and the oxidation of C1 intermediate species by absorbing -OH at low potential [11,31]. In addition, Co and Ni also benefit the modulations of the electronic structure of HEAs to promote the stability of the intermediates [5,29,52,55]. Therefore, the adsorption energy of reactants and intermediates can be changed by the interactions between different elements and the electronic structure of catalyst, so as to improve the catalytic reaction efficiency.

In order to explore the universality of PtRuRhCoNi NWs/C in alcohol oxidation reactions, we also studied the electrocatalytic performance of PtRuRhCoNi NWs/C for MOR in alkaline media. For MOR in alkaline medium, PtRuRhCoNi NWs/C showed significantly higher geometric area activity (69.5 mA cm^{-2}), mass activity (6.65 A mg^{-1}_{PtRuRh}, 8.20 A mg^{-1}_{Pt}) and specific activity (6.56 mA cm^{-2}_{PtRuRh}) than PtRuRh-CoNi NPs/C (60.2 mA cm^{-2}, 6.07 A mg^{-1}_{PtRuRh}, 5.66 mA cm^{-2}_{PtRuRh}), Pt NWs/C (55.8 mA cm^{-2}, 2.6 A mg^{-1}_{Pt}, 3.6 mA cm^{-2}_{Pt}), commercial Pt/C (55.1 mA cm^{-2}, 1.9 A mg^{-1}_{Pt}, 2.9 mA cm^{-2}_{Pt}) and recent alkaline MOR catalysts (Figs. S16 **a-d** and Table S6). After 2000 CV cycles, the mass

activity of the PtRuRhCoNi NWs/C maintained 90.2%, which was higher than that of PtRuRhCoNi NPs/C (89.1%), Pt NWs/C (84.6%) and commercial Pt/C (72.6%) (Figs. S16e and S17). In addition, after 1 h electrolysis, the mass activity of the PtRuRhCoNi NWs/C was 0.96 A mg^{-1}_{PtRuRh}, while the PtRuRhCoNi NPs/C, Pt NWs/C and commercial Pt/C were 0.59 A mg^{-1}_{PtRuRh}, 0.35 A mg^{-1}_{Pt} and 0.15 A mg^{-1}_{Pt} (Fig. S16f). These results indicate that PtRuRhCoNi NWs/C catalyst has excellent activity and durability in the alcohol oxidation reaction.

3.3. Electrocatalytic performance for HER

To demonstrate the multifunction of PtRuRhCoNi NWs/C, we also tested the HER performance in acidic and alkaline media. In 0.5 M H_2SO_4, PtRuRhCoNi NWs/C showed 13 mV overpotential at 10 mA cm^{-2} current density, which is lower than PtRuRhCoNi NPs/C (16 mV), Pt NWs/C (26 mV) and commercial Pt/C (30 mV) (Fig. 4a). The ECSAs of PtRuRhCoNi NWs/C, PtRuRhCoNi NPs/C, Pt NWs/C and commercial Pt/C were 89.9 m^2 g^{-1}_{PtRuRh}, 83.8 m^2 g^{-1}_{PtRuRh}, 77.5 m^2 g^{-1}_{Pt} and 73.2 m^2 g^{-1}_{Pt}, respectively (Table S1). To further characterize the activity of the catalyst, the current density was normalized by ECSA (Fig. 4b). At -0.025 V and -0.05 V *vs.* RHE, PtRuRhCoNi NWs/C exhibited an extremely high specific activity (3.86 mA cm^{-2}_{PtRuRh} and 9.87 mA cm^{-2}_{PtRuRh}), which was higher than PtRuRhCoNi NPs/C, Pt NWs/C and commercial Pt/C (Fig. 4c). At the same time, PtRuRhCoNi NWs/C also demonstrated high HER activity when normalized by noble metal mass (Fig. 4d). The mass activity of PtRuRhCoNi NWs/C was as high as 11.99 A mg^{-1}_{PtRuRh} (14.86 A mg^{-1}_{Pt}) at -0.05 V *vs.* RHE (Fig. 4e and Table S4), which was higher than PtRuRhCoNi NPs/C (10.61 A mg^{-1}_{PtRuRh}, 12.79 A mg^{-1}_{Pt}), Pt NWs/C (3.22 A mg^{-1}_{Pt}), commercial Pt/C (1.29 A mg^{-1}_{Pt}) and some ever-reported acidic HER catalysts (Table S7). To better understand the intrinsic activity of PtRuRhCoNi NWs/C, we further studied the TOF, Tafel slope and the electrochemical impedance spectroscopy (EIS) of the catalyst. As shown in Fig. 4f, PtRuRhCoNi NWs/C showed higher TOF than PtRuRhCoNi NPs/C, Pt NWs/C and commercial Pt/C. At 50 mV overpotential, the TOF value of PtRuRhCoNi NWs/C was 31.9 s^{-1}, which was 1.07, 4.19 and 7.52 times those of PtRuRhCoNi NPs/C (29.6 s^{-1}), Pt NWs/C (7.61 s^{-1}) and commercial Pt/C (4.24 s^{-1}). In addition, the four catalysts have a similar number of active sites (Fig. S18), combined with the high performance
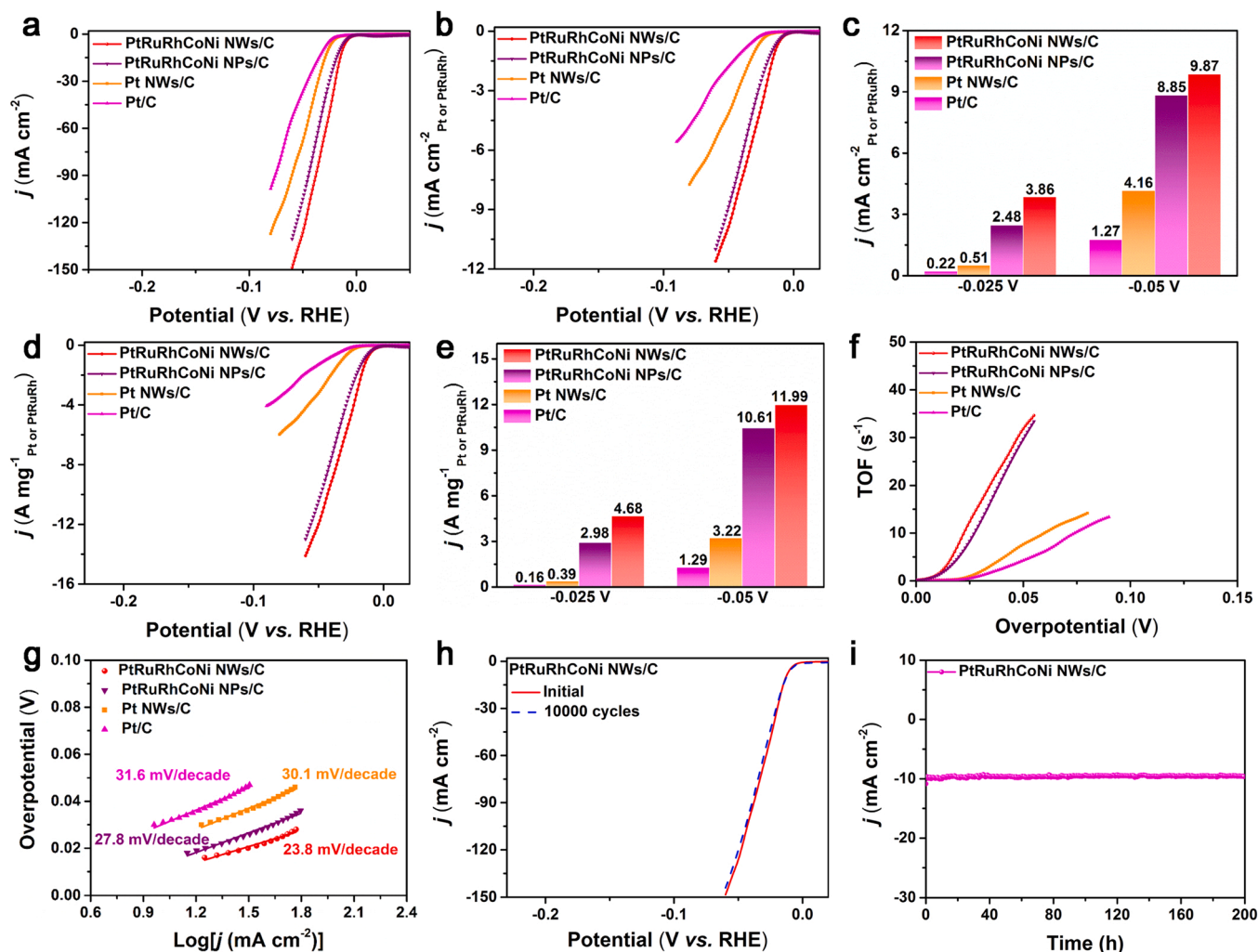
Fig. 4. HER performance of different electrocatalysts in 0.5 M H_2SO_4 solution. (a) Geometric area normalized LSV curves. (b) ECSA normalized LSV curves. (c) Comparisons of specific activities at different potentials. (d) Noble-metal mass normalized LSV curves. (e) Comparisons of mass activities at different potentials. (f) TOF. (g) Tafel slopes. (h) 10,000 CV cycles test, and (i) Long time CA curve of PtRuRhCoNi NWs/C.

of PtRuRhCoNi NWs/C, it can also indicate that the PtRuRhCoNi NWs/C catalyst has the highest intrinsic activity. As can be seen from Fig. 4g, the Tafel slope of PtRuRhCoNi NWs/C is 23.8 mV dec^{-1}, which is lower than PtRuRhCoNi NPs/C (27.8 mV dec^{-1}), Pt NWs/C (30.1 mV dec^{-1}) and commercial Pt/C (31.6 mV dec^{-1}), indicating that HER is the Volmer-Tafel mechanism [32]. In addition, from the Fig. S19, the EIS of PtRuRhCoNi NWs/C was significantly smaller than those of PtRuRhCoNi NPs/C, Pt NWs/C and commercial Pt/C, indicating that PtRuRhCoNi NWs/C had fast HER dynamics. These results indicate that PtRuRhCoNi NWs/C catalyst has excellent electrocatalytic performance of HER. The excellent HER performance may be attributed to the interactions between different elements in the HEAs, which can adjust the electronic structure and adsorption energy of the catalyst. In previous reports, Pt, Ru and Rh have excellent HER performance [26,32,56,57]. In addition, Co and Ni atoms can effectively adjust the electronic structure of HEA to improve the electrocatalytic performance [24,29].

We further evaluated the stability of the catalyst in the acidic solution. PtRuRhCoNi NWs/C catalyst showed almost no decay after 10,000 cycles (Fig. 4h) and no change in overpotential at 10 mA cm^{-2}. However, the polarization curve of PtRuRhCoNi NPs/C displayed decay after 10,000 cycles with overpotentials 19 mV at 10 mA cm^{-2} (Fig. S20a). The Pt NWs/C and commercial Pt/C showed significant attenuation after 1000 cycles (Figs. S20b-c), with overpotentials of 31 mV and 37 mV at 10 mA cm^{-2}, respectively. As shown in Fig. 4i, the current density of

PtRuRhCoNi NWs/C can be maintained above 93% after 200 h long-term stability test in 0.5 M H_2SO_4 solution. In addition, TEM and HRTEM images (Fig. S21), XRD (Fig. S22) results show that the morphology of PtRuRhCoNi NWs/C is well maintained without obvious agglomeration and no apparent destruction of crystallinity. And the element ratio of the catalyst did not obviously change (Table S3). In contrast, the current densities of PtRuRhCoNi NPs/C was maintained at 80% after 200 h (Fig. S20d). However, the current densities of Pt NWs/C and commercial Pt/C catalysts showed a significant decay trend after 12 h of testing (Fig. S20e and f). In addition, we also compared the catalytic performance of PtRuRhCoNi NWs and PtRuRhCoNi NWs/C for HER. From Fig. S23, the initial HER activities of the two catalysts are close. However, the activity of the PtRuRhCoNi NWs catalyst decayed after 10,000 cycles, and the NWs agglomerated. These results demonstrate the excellent stability of PtRuRhCoNi NWs/C catalyst.

For 1 M KOH solution, the prepared PtRuRhCoNi NWs/C catalyst also showed excellent HER activity and stability (Fig. S24). The overpotential of PtRuRhCoNi NWs/C obtained at 10 mA cm^{-2} current density was only 15 mV, lower than PtRuRhCoNi NPs/C (18 mV), Pt NWs/C (55 mV) and commercial Pt/C (60 mV) (Fig. S24a). And, the mass activity and specific activity of PtRuRhCoNi NWs/C were higher than those of PtRuRhCoNi NPs/C, Pt NWs/C, commercial Pt/C and some ever-reported alkaline HER catalysts (Fig. S24b-e, Table S4, and Table S8). At −0.05 V *vs.* RHE, PtRuRhCoNi NWs/C displayed high mass

activity (8.07 A mg$_{PtRuRh}^{-1}$, 9.95 A mg$_{Pt}^{-1}$) and specific activity (7.79 mA cm$_{PtRuRh}^{-2}$). Furthermore, in order to reveal the intrinsic activity of the electrocatalyst, we also tested the TOF, Tafel slope and EIS. The PtRuRhCoNi NWs/C catalyst showed better intrinsic activity than Pt NWs/C and commercial Pt/C. The PtRuRhCoNi NWs/C has a TOF of 26.7 s^{-1} at 50 mV overpotential, which was higher than PtRuRhCoNi NPs/C (17.4 s^{-1}), Pt NWs/C (1.1 s^{-1}) and commercial Pt/C (0.9 s^{-1}) (Fig. S24f). The Tafel slope of PtRuRhCoNi NWs/C was 26.1 mV dec^{-1}, lower than PtRuRhCoNi NPs/C, Pt NWs/C and commercial Pt/C. The results indicate that the catalyst has faster HER kinetics. As shown in Fig. S25, PtRuRhCoNi NWs/C catalyst exhibits a smaller semicircular diameter than PtRuRhCoNi NPs/C, Pt NWs/C and commercial Pt/C, indicating enhanced electron transfer capability. At the same time, PtRuRhCoNi NWs/C was tested for 10,000 cycles and 200 h of long-term stability at 10 mA cm^{-2} (Fig. S24h and i). The overpotential and current density did not change significantly. Importantly, the morphology and element ratio of PtRuRhCoNi NWs/C catalyst also remained unchanged (Fig. S26, Table S3). In contrast, the overpotential and current density of PtRuRhCoNi NPs/C decay after 10,000 cycles and 200 h stability (Fig. S27 a and d). However, the overpotential of Pt NWs/C and commercial Pt/C catalysts significantly increased and the current density decreased after 1000 cycles and 12 h tests (Fig. S27). The experimental results show that PtRuRhCoNi NWs/C HEA catalyst shows excellent HER performance in both alkaline and acidic media, which proves that the prepared high entropy alloy material has a wider application.

3.4. Density functional theory (DFT) calculation analysis

To understand the electrochemical performances of the PtRuRhCoNi HEA NWs, DFT calculations have been introduced to investigate the electronic structures as well as the reaction trends. Fig. 5a-b represent the electronic distributions of the HEA NWs regarding the bonding (blue isosurface) and anti-bonding (green isosurface) orbitals near the Fermi level (EF). Due to the multi-component in the PtRuRhCoNi-HEA, the interactions between different elements lead to the strong coupling between bonding and anti-bonding orbitals, which not only demonstrate the efficient site-to-site electron transfer but also supply varied active sites for different electrocatalysis reactions. Such interactions lead to the optimizations of the electronic structures, enabling both oxidation and reduction capability for EOR and HER, respectively. Notably, the bonding orbitals have been mainly focused on surface edge sites with lower coordination numbers. In comparison, the distributions of bonding and anti-bonding orbitals are highly ordered on the Pt surface. This indicates that the electroactivity and active sites on the Pt surface are relatively fixed, which limits their performances as multi-functional electrocatalysts for both oxidation and reduction processes. Detailed contributions to the electronic structures have been demonstrated through the projected partial density of states (PDOSs) (Fig. 5c). It is noted that all the orbitals from different elements lead to strong overlapping, amplifying the orbital coupling through the self-complementary effect. This maximizes the site-to-site electron transfer efficiency within the HEA to reach efficient electrocatalysis. Meanwhile, the D-band center also reveals the electronic structure balance induced by different elements (Fig. 5d). Notably, the D-band center of Rh-4d is highly consistent with the HEA. Other elements with higher and lower D-band centers guarantee both the oxidation and reduction capability of the HEA for both EOR and HER. From the bulk to the surface, Pt-5d exhibits the nearly linear increase trend, supporting the improved
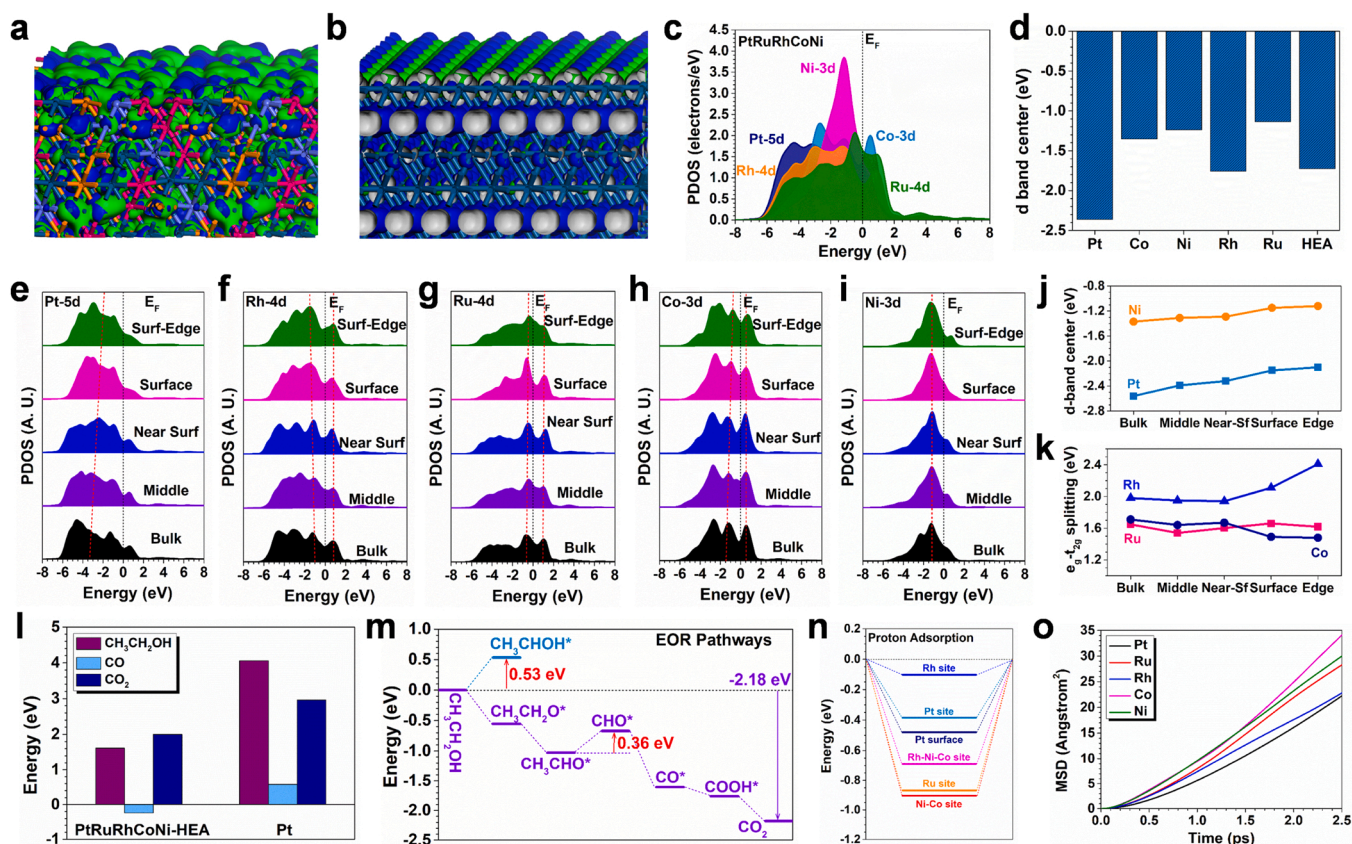

Fig. 5. The 3D contour plot of electronic distribution near Fermi level of (a) PtRuRhCoNi-HEA and (b) Pt. Dark green balls = Pt, purple balls = Ru, orange balls = Rh, blue balls = Co and pink balls = Ni. Blue isosurface = bonding orbitals and green isosurface = anti-bonding orbitals. (c) The PDOS of PtRuRhCoNi-HEA. (d) The D-band center comparison between individual elements and HEA. The site-dependent PDOS of (e) Pt-5d, (f) Rh-4d, (g) Ru-4d, (h) Co-3d and (i) Ni-3d. (j) The D-band center variations of Pt and Ni. (k) The e$_g$-t$_{2g}$ splitting variations of Ru, Rh, and Co. (l) The adsorption energy comparisons of CH$_3$CH$_2$OH, CO, and CO$_2$. (m) The energy change of ethanol oxidation. (n) The binding energy comparisons of the proton. (o) The mean square displacements of different elements in HEA.

electroactivity (Fig. 5e). Based on the self-complementary effect, the e_g-t_{2g} of Rh-4d orbitals display the gradually enlarged splitting from the bulk to the surface (Fig. 5f). This opposite trend to the Pt-5d enables the stabilization of the electroactivity in HEA to achieve durable electrocatalysis. In comparison, the e_g-t_{2g} splitting of both Ru-4d and Co-3d orbitals have not been significantly perturbed, remaining the similar valence states to promote the electron transfer (Fig. 5g-h). Ni-3d orbitals display the evident peak at E_V-1.20 eV ($E_V = 0$ eV), which has been well preserved even on the HEA surface (Fig. 5i). This sharp peak is critical to maintain the high selectivity towards specific intermediates. Although the dominant peak of Ni remains unchanged, the sharper peak causes a gradual increase in the D-band center (Fig. 5j). Pt-5d shows a similar upshifting trend of the D-band center, indicating the higher electroactivity of the HEA surface originates from the Pt and Ni sites. Both Ru-4d and Co-3d display a limited fluctuation on the e_g-t_{2g} splitting, leading to highly stable valence states on Ru and Co sites (Fig. 5k). Rh-4d orbitals exhibit the enlarged e_g-t_{2g} splitting, which strengthens the orbital coupling effect to guarantee the electron transfer on the surface. Then, the PtRuRhCoNi HEA also shows a superior adsorption preference for the key reactants and intermediates than the Pt surface (Fig. 5l). The stronger binding towards CH_3CH_2OH and CO_2 than Pt surface is the key factor to reach the efficient EOR process. The energy change of the EOR process has been also demonstrated (Fig. 5m). Due to evident energy barrier difference, the initial dehydrogenation of CH_3CH_2OH leads to the conversion from CH_3CH_2OH to CH_3CH_2O *. The following dehydrogenation shows a downhill trend until the formation of CH_3CHO *. The dissociation to generate CO * induces a small energy barrier of 0.36 eV. For the oxidation of CO towards CO_2, the reaction process is highly energetically favorable, releasing the energy of 2.18 eV for EOR. For the acidic HER process, we notice that Rh sites of HEA have shown more optimal adsorption energy to the zero line than the pristine Pt surface, resulting in the improved HER performance (Fig. 5n). In the end, we have investigated the dynamic of different elements in HEA (Fig. 5o). Notably, the high concentration Pt and Rh have shown much lower mean square displacements than that of Ru, Co, and Ni, which guarantee the stability of HEA nanowires and enable the long durability of HEA electrocatalyst.

4. Conclusions

In conclusion, we have successfully synthesized ultrathin PtRuRhCoNi HEA NWs, as the multifunctional electrocatalyst, exhibiting excellent EOR, MOR and HER properties and durability in acidic and alkaline solutions, which may be attributed to the optimized electronic structure of the HEA by strong self-complementary effect. For alcohol oxidation, the PtRuRhCoNi NWs/C achieve EOR activity of 7.68 A mg_{PtRuRh}^{-1} (9.50 A mg_{Pt}^{-1}) and 78% C1 selectivity (the highest C1 selectivity among the reported EOR catalysts, Table S5), MOR activity of 6.65 A mg_{PtRuRh}^{-1} (8.20 A mg_{Pt}^{-1}) in alkaline solution (one of the best MOR catalysts, Table S6), which are higher than those of PtRuRhCoNi NPs/C, Pt NWs/C and commercial Pt/C, respectively. In addition, the PtRuRhCoNi NWs/C also showed high EOR activity in an acidic solution. For HER, the PtRuRhCoNi NWs/C displayed only 13 and 15 mV overpotential with ultrahigh TOF values in 0.5 M H_2SO_4 and 1 M KOH solutions, respectively. And the PtRuRhCoNi NWs/C reached 11.99 A mg_{PtRuRh}^{-1} (14.86 A mg_{Pt}^{-1}), 9.87 mA cm_{PtRuRh}^{-2} (0.5 M H_2SO_4) and 8.07 A mg_{PtRuRh}^{-1} (9.95 A mg_{Pt}^{-1}), 7.79 mA cm_{PtRuRh}^{-2} (1 M KOH) high activity at −0.05 V *vs.* RHE (one of the best HER catalysts, Table S7 and Table S8), which were higher than those of PtRuRhCoNi NPs/C, Pt NWs/C and commercial Pt/C. In addition, the PtRuRhCoNi NWs/C showed excellent stability towards alcohol oxidation and HER in both acidic and alkaline solutions. DFT calculations have indicated that the electronic structure of the HEA shows a strong self-complementary effect. The opposite evolution trends of different metals not only achieve the robust electroactivity for both oxidation and reduction processes but also guarantee the stable lattice structure for durable electrocatalysis. This work provides a new strategy for the design of multifunctional catalysts with high catalytic activity, durability and selectivity, which can also be extended to other materials and catalysis fields.

CRediT authorship contribution statement

Hongdong Li and **Jianping Lai** designed the experiments. **Hongdong Li** performed most of the experiments and data analysis. **Bolong Huang** and **Mingzi Sun** performed the DFT calculations and mechanistic analysis. **Yue Pan** and **Juan Xiong** prepared the electrodes and helped with electrochemical measurements. **Zhenjiang Li**, **Yaodong Yu** and **Haoyang Du** helped analyze physical characterization data. **Lei Wang**, **Jianping Lai** and **Shouhua Feng** supervised the research. **Jianping Lai** conceived the research. All authors discussed the results and commented on the manuscript.

Declaration of Competing Interest

The authors declare that they have no known competing financial interests or personal relationships that could have appeared to influence the work reported in this paper.

Acknowledgement

Appendix A. Supporting information

Supplementary data associated with this article can be found in the online version at doi:10.1016/j.apcatb.2022.121431.

References

[1] R. Subbaraman, D. Tripkovic, D. Strmcnik, K.-C. Chang, M. Uchimura, A. P. Paulikas, V. Stamenkovic, N.M. Markovic, Enhancing hydrogen evolution activity in water splitting by tailoring Li$^+$-Ni(OH)$_2$-Pt interfaces (https://www.science.org/cgi/doi/), Science 334 (2011) 1256–1260, https://doi.org/10.1126/science.1211934.

[2] J. Zhu, L. Hu, P. Zhao, L.Y.S. Lee, K.-Y. Wong, Recent advances in electrocatalytic hydrogen evolution using nanoparticles, Chem. Rev. 120 (2020) 851–918, https://doi.org/10.1021/acs.chemrev.9b00248.

[3] G. Yang, Q. Zhang, H. Yu, F. Peng, Platinum-based ternary catalysts for the electrooxidation of ethanol, Particuology 58 (2021) 169–186, https://doi.org/10.1016/j.partic.2021.01.007.

[4] K. Yin, Y. Chao, F. Lv, L. Tao, W. Zhang, S. Lu, M. Li, Q. Zhang, L. Gu, H. Li, S. Guo, One nanometer PtIr nanowires as high-efficiency bifunctional catalysts for electrosynthesis of ethanol into high value-added multicarbon compound coupled with hydrogen production, J. Am. Chem. Soc. 143 (2021) 10822–10827, https://doi.org/10.1021/jacs.1c04626.

[5] W. Wang, X. Chen, X. Zhang, J. Ye, F. Xue, C. Zhen, X. Liao, H. Li, P. Li, M. Liu, Q. Kuang, Z. Xie, S. Xie, Quatermetallic Pt-based ultrathin nanowires intensified by Rh enable highly active and robust electrocatalysts for methanol oxidation, Nano Energy 71 (2020), 104623, https://doi.org/10.1016/j.nanoen.2020.104623.

[6] D.-J. Chen, Y.J. Tong, Irrelevance of carbon monoxide poisoning in the methanol oxidation reaction on a PtRu electrocatalyst, Angew. Chem. Int. Ed. 54 (2015) 9394–9398, https://doi.org/10.1002/anie.201503917.

[7] Y. Wang, S. Zou, W.-B. Cai, Recent advances on electro-oxidation of ethanol on Pt- and Pd-Based catalysts: From reaction mechanisms to catalytic materials, Catalysts 5 (2015) 1507–1534, https://doi.org/10.3390/catal5031507.

[8] C. Zhu, B. Lan, R.-L. Wei, C.-N. Wang, Y.-Y. Yang, Potential-dependent selectivity of ethanol complete oxidation on Rh electrode in alkaline media: A synergistic study of electrochemical ATR-SEIRAS and IRAS, ACS Catal. 9 (2019) 4046–4053, https://doi.org/10.1021/acscatal.9b00138.

[9] Q. Chang, S. Kattel, X. Li, Z. Liang, B.M. Tackett, S.R. Denny, P. Zhang, D. Su, J. G. Chen, Z. Chen, Enhancing C-C bond scission for efficient ethanol oxidation using PtIr nanocube electrocatalysts, ACS Catal. 9 (2019) 7618–7625, https://doi.org/10.1021/acscatal.9b02039.

[10] H. Liu, J. Li, L. Wang, Y. Tang, B.Y. Xia, Y. Chen, Trimetallic PtRhNi alloy nanoassemblies as highly active electrocatalyst for ethanol electrooxidation, Nano Res 10 (2017) 3324–3332, https://doi.org/10.1007/s12274-017-1545-z.

[11] S.-H. Han, H.-M. Liu, P. Chen, J.-X. Jiang, Y. Chen, Porous trimetallic PtRhCu cubic nanoboxes for ethanol electrooxidation, Adv. Energy Mater. 8 (2018), 1801326, https://doi.org/10.1002/aenm.201801326.

[12] J. Huang, Y. Liu, M. Xu, C. Wan, H. Liu, M. Li, Z. Huang, X. Duan, X. Pan, Y. Huang, PtCuNi tetrahedra catalysts with tailored surfaces for efficient alcohol oxidation, Nano Lett. 19 (2019) 5431–5436, https://doi.org/10.1021/acs.nanolett.9b01937.

[13] Z. Liang, L. Song, S. Deng, Y. Zhu, E. Stavitski, R.R. Adzic, J. Chen, J.X. Wang, Direct 12-electron oxidation of ethanol on a ternary Au(core)-PtIr(shell) electrocatalyst, J. Am. Chem. Soc. 141 (2019) 9629–9636, https://doi.org/10.1021/jacs.9b03474.

[14] Y. Lu, W. Wang, X. Chen, Y. Zhang, Y. Han, Y. Cheng, X.-J. Chen, K. Liu, Y. Wang, Q. Zhang, S. Xie, Composition optimized trimetallic PtNiRu dendritic nanostructures as versatile and active electrocatalysts for alcohol oxidation, Nano Res 12 (2019) 651–657, https://doi.org/10.1007/s12274-019-2273-3.

[15] Y. Zhu, L. Bu, Q. Shao, X. Huang, Subnanometer PtRh nanowire with alleviated poisoning effect and enhanced C-C bond cleavage for ethanol oxidation electrocatalysis, ACS Catal. 9 (2019) 6607–6612, https://doi.org/10.1021/acscatal.9b01375.

[16] F. Lv, W. Zhang, M. Sun, F. Lin, T. Wu, P. Zhou, W. Yang, P. Gao, B. Huang, S. Guo, Au clusters on Pd nanosheets selectively switch the pathway of ethanol electrooxidation: Amorphous/crystalline interface matters, Adv. Energy Mater. 11 (2021), 2100187, https://doi.org/10.1002/aenm.202100187.

[17] H. Peng, J. Ren, Y. Wang, Y. Xiong, Q. Wang, Q. Li, X. Zhao, L. Zhan, L. Zheng, Y. Tang, Y. Lei, One-stone, two birds: alloying effect and surface defects induced by Pt on Cu2−xSe nanowires to boost C-C bond cleavage for electrocatalytic ethanol oxidation, Nano Energy 88 (2021), 106307, https://doi.org/10.1016/j.nanoen.2021.106307.

[18] B. Lan, Q.-L. Wang, Z.-X. Ma, Y.-J. Wu, X.-L. Jiang, W.-S. Jia, C.-X. Zhou, Y.-Y. Yang, Efficient electrochemical ethanol-to-CO2 conversion at rhodium and bismuth hydroxide interfaces, Appl. Catal. B Environ. 300 (2022), 120728, https://doi.org/10.1016/j.apcatb.2021.120728.

[19] S.L. Zhang, X.F. Lu, Z.-P. Wu, D. Luan, X.W. Lou, Engineering platinum-cobalt nano-alloys in porous nitrogen-doped carbon nanotubes for highly efficient electrocatalytic hydrogen evolution, Angew. Chem. Int. Ed. 60 (2021) 19068–19073, https://doi.org/10.1002/anie.202106547.

[20] I.C. Gerber, P. Serp, A theory/experience description of support effects in carbon-supported catalysts, Chem. Rev. 120 (2020) 1250–1349, https://doi.org/10.1021/acs.chemrev.9b00209.

[21] D. Strmcnik, P.P. Lopes, B. Genorio, V.R. Stamenkovic, N.M. Markovic, Design principles for hydrogen evolution reaction catalyst materials, Nano Energy 29 (2016) 29–36, https://doi.org/10.1016/j.nanoen.2016.04.017.

[22] X. Wang, Y. Zheng, W. Sheng, Z.J. Xu, M. Jaroniec, S.Z. Qiao, Strategies for design of electrocatalysts for hydrogen evolution under alkaline conditions, Mater. Today 36 (2020) 125–138, https://doi.org/10.1016/j.mattod.2019.12.003.

[23] D. Zheng, L. Yu, W. Liu, X. Dai, X. Niu, W. Fu, W. Shi, F. Wu, X. Cao, Structural advantages and enhancement strategies of heterostructure water-splitting electrocatalysts, Cell Rep. Phys. Sci. 2 (2021), 100443, https://doi.org/10.1016/j.xcrp.2021.100443.

[24] H. Li, J. Lai, Z. Li, L. Wang, Multi-sites electrocatalysis in high-entropy alloys, Adv. Funct. Mater. 31 (2021) 2106715, https://doi.org/10.1002/adfm.202106715.

[25] J. Zhang, X. Qu, Y. Han, L. Shen, S. Yin, G. Li, Y. Jiang, S. Sun, Engineering PtRu bimetallic nanoparticles with adjustable alloying degree for methanol electrooxidation: enhanced catalytic performance, Appl. Catal. B Environ. 263 (2019) 118345, https://doi.org/10.1016/j.apcatb.2019.118345.

[26] S.-Y. Bae, J. Mahmood, I.-Y. Jeon, J.-B. Baek, Recent advances in ruthenium-based electrocatalysts for the hydrogen evolution reaction, Nanoscale Horiz. 5 (2020) 43–56, https://doi.org/10.1039/C9NH00485H.

[27] B. Tang, X. Yang, Z. Kang, L. Feng, Crystallized RuTe2 as unexpected bifunctional catalyst for overall water splitting, Appl. Catal. B: Environ. 278 (2020), 119281, https://doi.org/10.1016/j.apcatb.2020.119281.

[28] H.-Y. Chen, H.-J. Niu, Z. Han, J.-J. Feng, H. Huang, A.-J. Wang, Simple fabrication of trimetallic platinum-nickel-cobalt hollow alloyed 3D multipods for highly boosted hydrogen evolution reaction, J. Colloid Interface Sci. 570 (2020) 205–211, https://doi.org/10.1016/j.jcis.2020.02.090.

[29] H. Li, Y. Han, H. Zhao, W. Qi, D. Zhang, Y. Yu, W. Cai, S. Li, J. Lai, B. Huang, L. Wang, Fast site-to-site electron transfer of high-entropy alloy nanocatalyst driving redox electrocatalysis, Nat. Commun. 11 (2020) 5437, https://doi.org/10.1038/s41467-020-19277-9.

[30] D. Zhang, Y. Shi, H. Zhao, W. Qi, X. Chen, T. Zhan, S. Li, B. Yang, M. Sun, J. Lai, B. Huang, L. Wang, The facile oil-phase synthesis of a multi-site synergistic high-entropy alloy to promote the alkaline hydrogen evolution reaction, J. Mater. Chem. A 9 (2021) 889–893, https://doi.org/10.1039/D0TA10574K.

[31] D. Wu, K. Kusada, T. Yamamoto, T. Toriyama, S. Matsumura, S. Kawaguchi, Y. Kubota, H. Kitagawa, Platinum-group-metal high-entropy-alloy nanoparticles,

[32] G. Feng, F. Ning, J. Song, H. Shang, K. Zhang, Z. Ding, P. Gao, W. Chu, D. Xia, Sub-2 nm ultrasmall high-entropy alloy nanoparticles for extremely superior electrocatalytic hydrogen evolution, J. Am. Chem. Soc. 143 (2021) 17117–17127, https://doi.org/10.1021/jacs.1c07643.

[33] C. Zhan, Y. Xu, L. Bu, H. Zhu, Y. Feng, T. Yang, Y. Zhang, Z. Yang, B. Huang, Q. Shao, X. Huang, Subnanometer high-entropy alloy nanowires enable remarkable hydrogen oxidation catalysis, Nat. Commun. 12 (2021) 6261, https://doi.org/10.1038/s41467-021-26425-2.

[34] A.-L. Wang, H.-C. Wan, H. Xu, Y.-X. Tong, G.-R. Li, Quinary PdNiCoCuFe alloy nanotube arrays as efficient electrocatalysts for methanol oxidation, Electrochim. Acta 127 (2014) 448–453, https://doi.org/10.1016/j.electacta.2014.02.076.

[35] T.A.A. Batchelor, J.K. Pedersen, S.H. Winther, I.E. Castelli, K.W. Jacobsen, J. Rossmeisl, High-entropy alloys as a discovery platform for electrocatalysis, Joule 3 (2019) 834–845, https://doi.org/10.1016/j.joule.2018.12.015.

[36] T. Löffler, A. Savan, A. Garzón-Manjón, M. Meischein, C. Scheu, A. Ludwig, W. Schuhmann, Toward a paradigm shift in electrocatalysis using complex solid solution nanoparticles, ACS Energy Lett. 4 (2019) 1206–1214, https://doi.org/10.1021/acsenergylett.9b00531.

[37] E.P. George, D. Raabe, R.O. Ritchie, High-entropy alloys, Nat. Rev. Mater. 4 (2019) 515–534, https://doi.org/10.1038/s41578-019-0121-4.

[38] S. Li, J. Wang, X. Lin, G. Xie, Y. Huang, H.-J. Qiu, Flexible solid-state direct ethanol fuel cell catalyzed by nanoporous high-entropy Al-Pd-Ni-Cu-Mo anode and spinel (AlMnCo)3O4 cathode, Adv. Funct. Mater. 31 (2021), 2007129, https://doi.org/10.1002/adfm.202007129.

[39] T. Yu, Y. Zhang, Y. Hu, K. Hu, X. Lin, G. Xie, X. Liu, K.M. Reddy, Y. Ito, H.-J. Qiu, Twelve-component free-standing nanoporous high-entropy alloys for multifunctional electrocatalysis, ACS Mater. Lett. 4 (2022) 181–189, https://doi.org/10.1021/acsmaterialslett.1c00762.

[40] Z. Jin, J. Lyu, K. Hu, Z. Chen, S. Xie, X. Liu, X. Lin, H.-J. Qiu, Eight-component nanoporous high-entropy oxides with low Ru contents as high-performance bifunctional catalysts in Zn-air batteries, Small 18 (2022), 2107207, https://doi.org/10.1002/smll.202107207.

[41] W. Zhang, Y. Yang, B. Huang, F. Lv, K. Wang, N. Li, M. Luo, Y. Chao, Y. Li, Y. Sun, Z. Xu, Y. Qin, W. Yang, J. Zhou, Y. Du, D. Su, S. Guo, Ultrathin PtNiM (M = Rh, Os, and Ir) nanowires as efficient fuel oxidation electrocatalytic materials, Adv. Mater. 31 (2019), 1805833, https://doi.org/10.1002/adma.201805833.

[42] L. Li, L. Bu, B. Huang, P. Wang, C. Shen, S. Bai, T.-S. Chan, Q. Shao, Z. Hu, X. Huang, Compensating electronic effect enables fast site-to-site electron transfer over ultrathin RuMn nanosheet branches toward highly electroactive and stable water splitting, Adv. Mater. 33 (2021), 2105308, https://doi.org/10.1002/adma.202105308.

[43] L. Bu, S. Guo, X. Zhang, X. Shen, D. Su, G. Lu, X. Zhu, J. Yao, J. Guo, X. Huang, Surface engineering of hierarchical platinum-cobalt nanowires for efficient electrocatalysis, Nat. Commun. 7 (2016) 11850, https://doi.org/10.1038/ncomms11850.

[44] K. Li, X. Li, H. Huang, L. Luo, X. Li, X. Yan, C. Ma, R. Si, J. Yang, J. Zeng, One-nanometer-thick PtNiRh trimetallic nanowires with enhanced oxygen reduction electrocatalysis in acid media: Integrating multiple advantages into one catalyst, J. Am. Chem. Soc. 140 (2018) 16159–16167, https://doi.org/10.1021/jacs.8b08836.

[45] H. Xu, H. Shang, C. Wang, Y. Du, Ultrafine Pt-based nanowires for advanced catalysis, Adv. Funct. Mater. 30 (2020), 2000793, https://doi.org/10.1002/adfm.202000793.

[46] R.-L. Zhang, J.-J. Duan, L.-P. Mei, J.-J. Feng, P.-X. Yuan, A.-J. Wang, Facile synthesis of porous iridium-palladium-plumbum wire-like nanonetworks with boosted catalytic performance for hydrogen evolution reaction, J. Colloid Interface Sci. 580 (2020) 99–107, https://doi.org/10.1016/j.jcis.2020.06.124.

[47] J.C. Stewart, D.S. Matthew, J.P. Chris, J.H. Phil, I.J.P. Matt, R. Keith, C.P. Mike, First principles methods using CASTEP, Z. Krist. Cryst. Mater. 220 (2005) 567–570, https://doi.org/10.1524/zkri.220.5.567.65075.

[48] J.P. Perdew, K. Burke, M. Ernzerhof, Generalized gradient approximation made simple, Phys. Rev. Lett. 77 (1996) 3865–3868, https://doi.org/10.1103/PhysRevLett.77.3865.

[49] P.J. Hasnip, C.J. Pickard, Electronic energy minimisation with ultrasoft pseudopotentials, Comput. Phys. Commun. 174 (2006) 24–29, https://doi.org/10.1016/j.cpc.2005.07.011.

[50] J.P. Perdew, J.A. Chevary, S.H. Vosko, K.A. Jackson, M.R. Pederson, D.J. Singh, C. Fiolhais, Atoms, molecules, solids, and surfaces: Applications of the generalized gradient approximation for exchange and correlation, Phys. Rev. B 46 (1992) 6671–6687, https://doi.org/10.1103/PhysRevB.46.6671.

[51] J.D. Head, M.C. Zerner, A broyden-fletcher-goldfarb-shanno optimization procedure for molecular geometries, Chem. Phys. Lett. 122 (1985) 264–270, https://doi.org/10.1016/0009-2614(85)80574-1.

[52] H. Li, Y. Pan, D. Zhang, Y. Han, Z. Wang, Y. Qin, S. Lin, X. Wu, H. Zhao, J. Lai, B. Huang, L. Wang, Surface oxygen-mediated ultrathin PtRuM (Ni, Fe, and Co) nanowires boosting methanol oxidation reaction, J. Mater. Chem. A 8 (2020) 2323–2330, https://doi.org/10.1039/C9TA11745H.

[53] N. Erini, V. Beermann, M. Gocyla, M. Gliech, M. Heggen, R.E. Dunin-Borkowski, P. Strasser, The effect of surface site ensembles on the activity and selectivity of ethanol electrooxidation by octahedral PtNiRh nanoparticles, Angew. Chem. Int. Ed. 56 (2017) 6533–6538, https://doi.org/10.1002/anie.201702332.

[54] S. Bai, Y. Xu, K. Cao, X. Huang, Selective ethanol oxidation reaction at the Rh-SnO2 interface, Adv. Mater. 33 (2020), 2005767, https://doi.org/10.1002/adma.202005767.

[55] L. Chen, L. Lu, H. Zhu, Y. Chen, Y. Huang, Y. Li, L. Wang, Improved ethanol electrooxidation performance by shortening Pd-Ni active site distance in Pd-Ni-P nanocatalysts, Nat. Commun. 8 (2017) 14136, https://doi.org/10.1038/ncomms14136.

[56] D. Cao, H. Xu, D. Cheng, Construction of defect-rich RhCu nanotubes with highly active Rh_3Cu_1 alloy phase for overall water splitting in all pH values, Adv. Energy Mater. 10 (2020), 1903038, https://doi.org/10.1002/aenm.201903038.

[57] M.-T. Chen, R.-L. Zhang, J.-J. Feng, L.-P. Mei, Y. Jiao, L. Zhang, A.-J. Wang, A facile one-pot room-temperature growth of self-supported ultrathin rhodium-iridium nanosheets as high-efficiency electrocatalysts for hydrogen evolution reaction, J. Colloid Interface Sci. 606 (2022) 1707–1714, https://doi.org/10.1016/j.jcis.2021.08.144.